Nanoscale

ROYAL SOCIETY OF CHEMISTRY

COMMUNICATION

View Article Online
View Journal

Cite this: DOI: 10.1039/d0nr08644d

Received 6th December 2020,
Accepted 6th February 2021

DOI: 10.1039/d0nr08644d

rsc.li/nanoscale

Single-mode lasing of $CsPbBr_3$ perovskite NWs enabled by the Vernier effect†

Fangtao Li,[a,b] Mingming Jiang,[c] Yang Cheng,[d] Yufei Zhang,[a] Zheng Yang,[a] Yiyao Peng,[a] Wenda Ma,[e] Qiushuo Chen,[a] Chunfeng Wang,[e] Kaihui Liu,[d] Rongming Wang,*[b] Junfeng Lu*[c] and Caofeng Pan*[a,f,d,g]

Inorganic lead halide perovskite ($CsPbX_3$, X = Cl, Br, I) NWs (NWs) have been employed in lasers due to their intriguing attributes of tunable wavelength, low threshold, superior stability, and easy preparation. However, current $CsPbX_3$ NW lasers usually work in a multi-mode modal, impeding their practical applications in optical communication due to the associated false signaling. In this work, high-performance single-mode lasing has been demonstrated by designing and fabricating coupled cavities in the high-quality single-crystal $CsPbBr_3$ NWs *via* the focused ion beam (FIB) milling approach. The single-mode laser shows a threshold of 20.1 μJ cm^{-2} and a high quality factor of ~2800 profiting from the Vernier effect, as demonstrated by the experiments and finite-different time-domain (FDTD) simulations. These results demonstrate the promising potentials of the $CsPbX_3$ NW lasers in optical communication and integrated optoelectronic devices.

Introduction

Miniaturized semiconductor lasers have attracted considerable attention due to their great potential in commercial applications such as optical communication, data storage, high-resolution imaging and sensing.[1–4] A myriad of lasers with nanoscale footprint have been demonstrated by the conjunction of novel materials and designed constructions since the first proposed nanolaser by optically pumping the single-crystalline zinc oxide NWs (NWs) in 2001,[5] among which the semiconductor NW lasers have been considered as a perspective candidate for the on-chip photonic devices because of their small footprint as well as the intrinsic combination of optical cavity and gain medium.[6–10] However, most of the semiconductor NW lasers present a multi-mode manner, hindering their practical applications due to the temporal pulse broadening and false signals caused by the group velocity dispersion.[2,11,12] The single-mode laser can avoid the aforementioned issue because of the stable output produced at one frequency, boosting their development in nanophotonic integrated devices.[13–17] In principle, single-mode lasers can be obtained when the free spectral range (FSR) is larger than the bandwidth of the optical gain.[11,13,18] In addition, a series of approaches including decreasing the cavity size, constructing distributed-Bragg-reflector (DBR) mirrors or distributed-feedback (DFB) gratings, and parity-time symmetry breaking have been proposed to obtain a single-mode laser.[11,17,19–24] For example, Wang *et al.* obtained GaN NW single mode lasers by shortening the length of the cavity.[11] In spite of these achievements, these methods suffer from the increased threshold caused by decreasing the cavity size or the processing complexity associated with the construction of DBR/DFB.[18,25]

Vernier effect is a well-known technique in passive systems to regulate laser modes, which has been recently applied to improve the monochromaticity of the laser, where the lasing modes, except for at the same frequency ones, are significantly suppressed due to the strong coupling of the adjacent optical cavity.[2,12,13] For example, Xu *et al.* realized a single-mode lasing output in comb-like ZnO microrod arrays *via* simultaneously exciting two adjacent ZnO microrods, but the coupled cavity cannot be precisely designed and controlled.[26] Focused ion beam (FIB) is a powerful tool for the ablation of materials, promising the design and fabrication of the coupled

---

[a] CAS Center for Excellence in Nanoscience Beijing Key Laboratory of Micro-nano Energy and Sensor, Beijing Institute of Nanoenergy and Nanosystems Chinese Academy of Sciences, Beijing 100083, P. R. China. E-mail: cfpan@binn.cas.cn
[b] Advanced Innovation Center for Materials Genome Engineering, Beijing Key Laboratory for Magneto-Photoelectrical Composite and Interface Science, School of Mathematics and Physics, University of Science and Technology Beijing, Beijing 100083, P.R. China. E-mail: rmwang@ustb.edu.cn
[c] College of Science, Nanjing University of Aeronautics and Astronautics, Nanjing 210016, P. R. China. E-mail: lujunfeng@nuaa.edu.cn
[d] State Key Laboratory for Mesoscopic Physics, Collaborative Innovation Centre of Quantum Matter, School of Physics, Peking University, Beijing 100871, P. R. China
[e] College of Physics and Optoelectronic Engineering, Shenzhen University, Shenzhen 518060, P. R. China
[f] School of Nanoscience and Technology, University of Chinese Academy of Sciences, Beijing 100049, P. R. China
[g] Center on Nanoenergy Research, School of Physical Science and Technology, Guangxi University, Nanning, Guangxi 530004, P. R. China

† Electronic supplementary information (ESI) available. See DOI: 10.1039/d0nr08644d

optical cavity in a precisely controlled manner.[2,27] On the other hand, lead halide perovskites have been employed in lasing devices due to their excellent optoelectronic properties such as direct band-gap, tunable band-gap, and high photoluminescence quantum yield.[8,28–34] Compared with the organic–inorganic perovskite NWs, the all-inorganic perovskite NWs showed better stability to light, heat, and moisture.[35,36] All-inorganic perovskite NWs can be conveniently prepared by solution or chemical vapor deposition (CVD) methods with the precise control of morphology, dimension, and component, which are critical for the laser.[37–42] Some perovskite-based single-mode lasers have been obtained.[43,44] However, to the best of our knowledge, single-mode lasers of all-inorganic perovskite NWs enabled by the Vernier effect have not been reported.

Herein, we synthesized high quality single crystal $CsPbBr_3$ perovskite NWs with smooth surface and triangle cross-section by a typical chemical vapor-phase method. The as-prepared $CsPbBr_3$ NWs enable a multi-mode F–P-type lasing under optical pumping at room temperature. Most importantly, the single-mode laser of $CsPbBr_3$ NWs was also achieved by designing and fabricating the coupling cavity in the as-prepared $CsPbBr_3$ NWs by integrating FIB milling and the Vernier effect, exhibiting a threshold of 20.1 μJ cm^{-2} and a high Q of ∼2800. This work provides a single-mode laser of perovskite NWs in an easy and controlled manner, promoting the application potential of perovskite NW lasers in optical communication, spectrum and other fields.

Results and discussion

The $CsPbBr_3$ NWs were grown on a mica substrate by a typical vapor-phase deposition method, as previously reported (details can be found in Experiment section and Fig. S1†).[43] The diameter and length of the $CsPbBr_3$ NWs can be well controlled by adjusting the reaction time; the longer the time, the larger the diameter and length, as shown in Fig. S2.† Fig. 1a and the inset show the scanning electron microscopy (SEM) images of the as-prepared $CsPbBr_3$ NWs with a growth time of 10 min, exhibiting the smooth surface, triangle cross-section, and a length of about 20–30 μm. The crystalline phase of the $CsPbBr_3$ perovskite NWs is generally determined by the synthesis temperature, where the cubic phase is preferred when the temperature is higher than 130 °C.[45,46] The X-ray powder diffraction (XRD) pattern of the $CsPbBr_3$ perovskite NWs is shown in Fig. 1b, with the 2θ locating at 15.1°, 21.6°, 30.6°, and 44.0°, corresponding to the (100), (110), (200) and (220) lattice planes of cubic-phase $CsPbBr_3$ perovskite, respectively.[47,48] The group of peaks marked with a blue star are assigned to the (002), (004), (006) and (008) lattice planes of the mica substrate.[46] Fig. 1c shows the room-temperature linear absorption (red line) and photoluminescence (PL, blue line) spectra of the $CsPbBr_3$ NWs. A clear absorption peak appeared at a wavelength of ∼523.0 nm, indicating the energy band-gap of 2.37 eV of the $CsPbBr_3$ NWs. Meanwhile, the full width at half maximum (FWHM) of the PL spectrum is 18.5 nm, which is smaller than the solution-processed $CsPbBr_3$ perovskites such as quantum dots and bulks.[23,45] The sharp XRD peaks and narrow FWHM demonstrate that the $CsPbBr_3$ NWs possess good crystal quality. The low-magnification TEM image (Fig. 1d) and EDX mappings (Fig. 1e–g) demonstrate that the Cs, Pb, Br, elements were homogeneously distributed in the triangle cross-section of the $CsPbBr_3$ NWs. Fig. 1h presents the high-resolution TEM image of the $CsPbBr_3$ NWs, with a 0.29 nm lattice spacing that corresponds to the (200) lattice plane of the cubic-phase $CsPbBr_3$ perovskite. Fig. 1i shows the selected area electron diffraction (SAED) image of the $CsPbBr_3$ NWs, confirming that the $CsPbBr_3$ NWs grew along the [001] direction.[39]

All the laser properties of the $CsPbBr_3$ NWs were characterized by a confocal system equipped with a femtosecond excitation source (λ_{ex} = 405 nm, ∼20 μm diameter, 190 fs pulse duration, and 1000 Hz repetition rate) at room temperature,

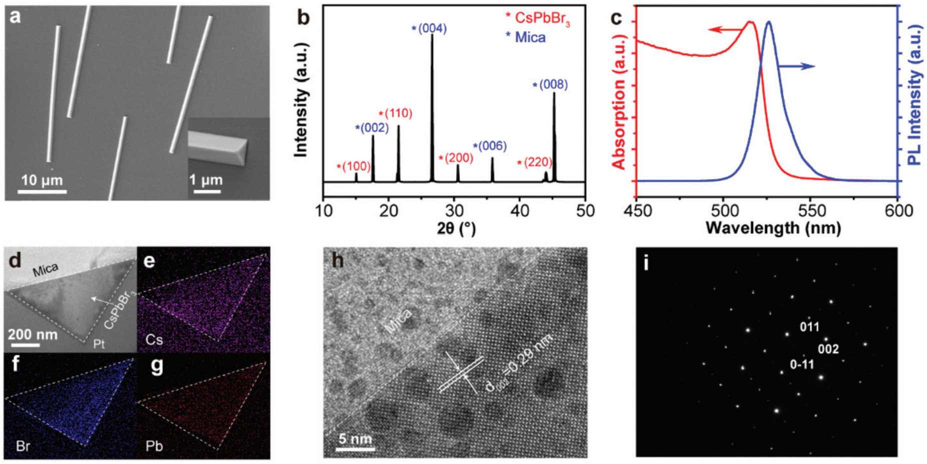

Fig. 1 The morphology and structural properties characterization of the as-prepared $CsPbBr_3$ NWs. (a) The low and high (inset) magnification SEM images of the $CsPbBr_3$ NWs. (b) The XRD patterns of $CsPbBr_3$ NWs. (c) The absorption (red line) and photoluminescence (blue line) spectra of NWs. (d) Low-resolution TEM image of the $CsPbBr_3$ NW's cross-section. (e–g) The EDX mappings of Cs, Br, and Pb elements distributed in the cross-section of the $CsPbBr_3$ NW, respectively. (h) High resolution TEM image and corresponding SAED patterns (i) of the $CsPbBr_3$ NW.

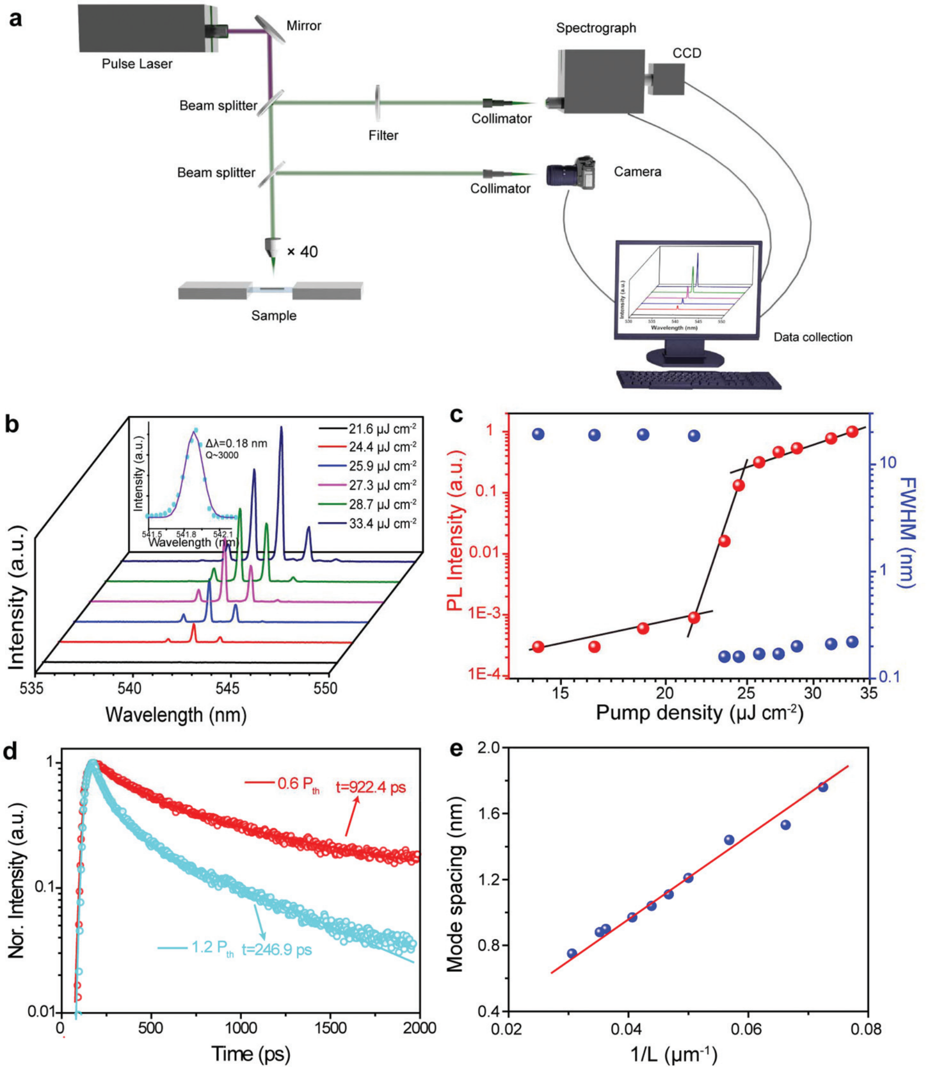

Fig. 2 Laser properties test of $CsPbBr_3$ NWs. (a) The schematic diagram of the optical testing system. (b) The pump-dependent PL spectra of the $CsPbBr_3$ NWs. Inset: Gaussian-fitted FWHM line of a lasing peak. (c) The integrated output intensity (red sphere) and FWHM (blue sphere) as functions of pumping density. (d) The fitted time-resolved spectra of the $CsPbBr_3$ NWs at the pumping density below (blue cycle) and above (red cycle) the lasing threshold, respectively. (e) The FSR as a function of $1/L$, where L is the length of $CsPbBr_3$ NWs.

and a ×40 objective lens was used to focus the pumping laser beam and collect the emitted light, as depicted in Fig. 2a. Fig. 2b shows the dependence of the emission spectra on the pumping power of an individual $CsPbBr_3$ NW with the length of ~18 μm. The spontaneous emission (SPE) spectrum located at 528.0 nm with the FWHM of about 18.0 nm is launched under a low pumping density of 21.6 μJ cm^{-2}. Moreover, sharp laser peaks emerged when the pumping density is increased to 24.4 μJ cm^{-2}, showcasing the improved intensity with the increased pumping density. The inset in Fig. 2b shows the Gaussian-fitted curve of a laser peak at the pumping density of 25.9 μJ cm^{-2}, indicating that the FWHM is 0.18 nm. The lasing quality factor (Q) of the $CsPbBr_3$ NW is about 3000, as evaluated by eqn (1):

$$Q = \lambda / \Delta\lambda \tag{1}$$

where λ is the emitted laser wavelength and $\Delta\lambda$ is the FWHM of the emitted laser peak.[16] This value is superior to a majority of the lasers with the $CsPbBr_3$ micro/NWs prepared by the solution method.[25,35] Fig. 2c displays the integrated output intensity (red sphere) and FWHM (blue sphere) as the functions of the pumping density. The fitting result of the integrated output intensity data is the anticipant S-curve model for lasing oscillation,[49] first knee indicating that the threshold pumping power (P_{th}) of the $CsPbBr_3$ NW is 22.8 μJ cm^{-2}. It can be found that the fluorescence intensity increases slowly when the pumping density is lower than P_{th}, and the fluorescence intensity dramatically increases when the pumping density is higher than P_{th}. Meanwhile, the FWHM decreases from ~18.0 nm to ~0.2 nm as well, demonstrating the transition from SPE to stimulated emission (SE). To further confirm the occurrence of laser behavior, the time-resolved photoluminescence (TRPL) measurement was performed by using a streak camera. Fig. 2d shows the lifetime curves below (blue cycle) and above (red cycle) the lasing threshold fitted with monoexponential functions; as expected, the lifetime is shortened from 924.4 ps to 245.9 ps when the pumping density exceeds the lasing threshold. The shortening of the lifetime can be attributed to the bimolecular recombination of the free charge carriers generated by Mott transition, which suggest the occurrence of laser behavior.[7,32,36,50] Moreover, this phenomenon was more clearly and intuitively confirmed by the streak-camera images, as shown in Fig. S4(a and b).† To determine the resonant mode of the $CsPbBr_3$ NW cavity, we investigated the relationship between FSR and the length of $CsPbBr_3$ NWs. Fig. 2e shows the FSR as a function of $1/L$, where L is the length of $CsPbBr_3$ NWs. We can see that the FSR linearly decreases with an increase in the length of the $CsPbBr_3$ NWs, which is consistent with the characteristics of F–P-type microcavity. According to eqn (2),

$$\mathrm{FSR} = \lambda^2/(2n_{\mathrm{g}}L) \tag{2}$$

the group refractive index (n_{g}) of the $CsPbBr_3$ NWs is about 5.9, which is in agreement with the previous studies.[39] To further confirm the F–P-type resonance cavity in the $CsPbBr_3$ NWs, we carried out an electrical field distribution simulation by the FDTD method. Fig. S5 (a and b)† present the two-dimensional (2D) normalized electric field intensity distribution at the length and the cross-section of a $CsPbBr_3$ NW. The simulation results reveal that the optical field is well confined in the NWs and the light leaks out from the pair of end facets, indicating a typically axial F–P-type microcavity resonance.[39]

As aforementioned, the Vernier effect is an efficient means to realize single-mode-lasing output in F–P-type cavities without reducing the cavity size. Moreover, FIB is a very powerful tool to prepare the one-dimensional NW coupled cavity because it can precisely define the ratio of the length and the width of the air-gap.[2] So, we selected FIB to fabricate the $CsPbBr_3$ NW coupled cavity. A protection layer of aluminum-doped zinc oxide (AZO) with a thickness of about 80 nm is deposited on $CsPbBr_3$ NWs before FIB milling to avoid NWs being destroyed during the FIB milling. Then, a 7.7 pA of Ga^{2+} beam current is used to mill the $CsPbBr_3$ NWs, and the width of air-gap can be well controlled by adjusting the milling parameters. The SEM image (Fig. S6†) of the end face of the $CsPbBr_3$ NWs demonstrates that the surface still remained smooth even after FIB milling. Fig. 3a shows the SEM image of a $CsPbBr_3$ NW with two milled cavities; one is of 15.72 μm named cavity-A, and the other one is of 10.62 μm named cavity-B. The higher magnification SEM image (Fig. 3b) indicates that the width of air-gap is ~60 nm. By moving the excitation spot, cavity-A and cavity-B can be individually and simultaneously excited. Fig. 3c shows the laser spectra of the coupled cavity, cavity-A and cavity-B, at a high pumping density ($>P_{\mathrm{th}}$). The inset is the optical photograph of the $CsPbBr_3$ NW, and the violet dash circle represents the position of the excitation spot. We can see that when only cavity-A is excited, there is a series of typical F–P lasing peaks that appear around 540 nm. A similar phenomenon is also observed in cavity-B. It is worth noting that one lasing peak located at ~539.70 nm co-exists in both the cavities and overlaps, which meets the condition for the occurrence of the Vernier effect. As expected, a single-mode laser was obtained at 540.39 nm when both cavity-A and cavity-B were simultaneously excited. To further confirm that the Vernier effect led to the generation of a single-mode lasing, we carefully analyzed the FSRs of cavity-A and cavity-B. According to eqn (2), FSR will decrease with the increase in the cavity length. The FSRs of cavity-A and cavity-B obtained from the lasing spectra are 1.6 nm and 2.5 nm, respectively, which are very close to the theoretical values. Previous reports demonstrated that the occurrence of the Vernier effect in two coupled cavities should satisfy eqn (3):

$$N\mathrm{FSR}_{\mathrm{A}} = M\mathrm{FSR}_{\mathrm{B}} \tag{3}$$

where N and M are integers.[26] As a result, the FSR of the coupled cavity will be enlarged, and the single-mode laser will be generated when the FSR is beyond the gain range. The mode numbers of cavity-A and cavity-B can be obtained by formula (4):

$$N = 2n_{\mathrm{g}}L/\lambda \tag{4}$$

as shown in Fig. 3c, which also indicates the occurrence of the Vernier effect. It is worth noting that the position of single-mode lasing does not correspond to cavity-A and cavity-B very well, which is ascribed to the phase delay.[2,13] Moreover, in order to explore the influence of the length ratio on the coupled cavity, we prepared two samples with different length ratios of 4 : 3 and 2 : 1, as shown in Fig. S7.† Unfortunately, some lasing peaks were suppressed, but neither of them achieved single-mode laser output. This suggests that the single-mode laser output realized by the Vernier effect need appropriate length ratio of cavities. Fig. 3d displays the pump-dependent PL spectra of the coupled cavity. We know that the coupling cavity always maintains the single-mode laser output with an increase in the pumping power, indicating the good stability of the coupled cavity. The side-mode suppression ratio (SMSR) is an important index to evaluate the quality of a single-mode laser, which can be calculated by formula (5):

$$\mathrm{SMSR} = 10\log(M_1/M_2) \tag{5}$$

where M_1 is the intensity of the dominant mode and M_2 is the intensity of the side mode.[15] The SMSR of the coupled cavity is 23.0 dB at the pumping density of 36.5 μJ cm^{-2}, which is better than the reported results such as 19.7 dB in ZnO comb-like structure, 16.7 dB in $CsPbBr_3$ microrods, and 15.6 dB in GaN NW-pair.[12,25,26] The inset in Fig. 3d shows the Gaussian fitted spectrum at a pumping density of 26.6 μJ cm^{-2}, demonstrating a FWHM of 0.18 nm, and a corresponding Q of ~2800. Fig. 3e shows the PL intensity (red sphere) and FWHM (blue sphere) as functions of the pumping density. The fitted PL intensity gives the threshold pumping power (P_{th}) as 20.1 μJ cm^{-2}

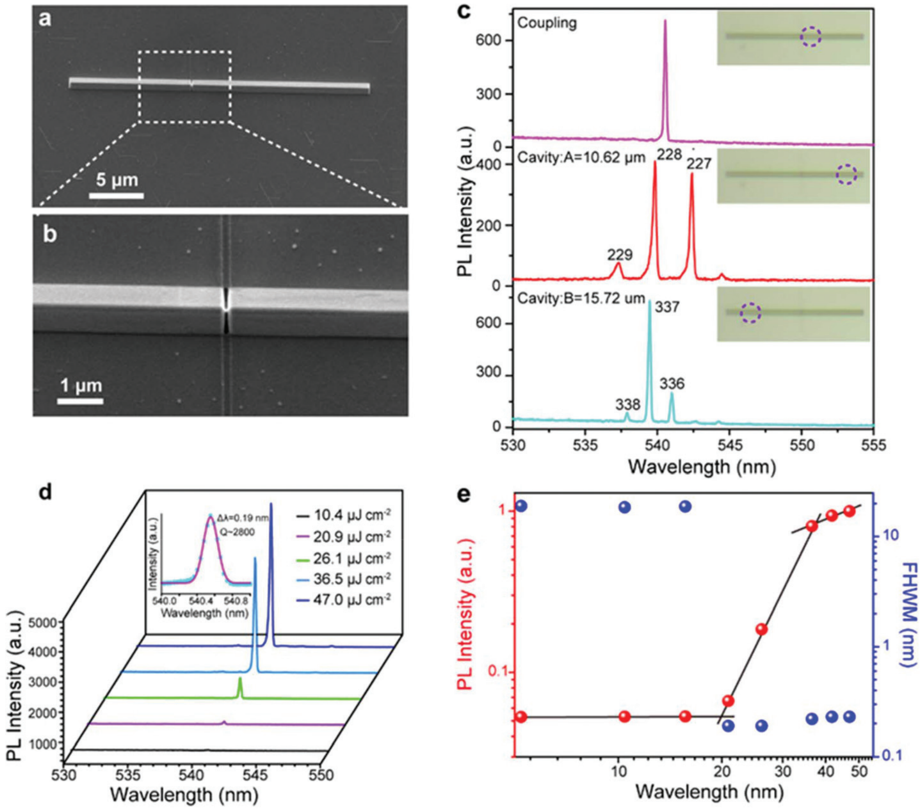

Fig. 3 The morphology and laser properties characterization of coupled cavity. (a and b) The low and high-magnification SEM images of coupled cavity, respectively. (c) The spectra of cavity-A, cavity-B and coupled cavity. Inset is the optical photograph of the coupled cavity. (d) The pumping power dependent PL spectra of the coupled cavity. Inset: Gaussian fitted FWHM line of a lasing peak. (e) The integrated output intensity (red sphere) and FWHM (blue sphere) as functions of pumping density.

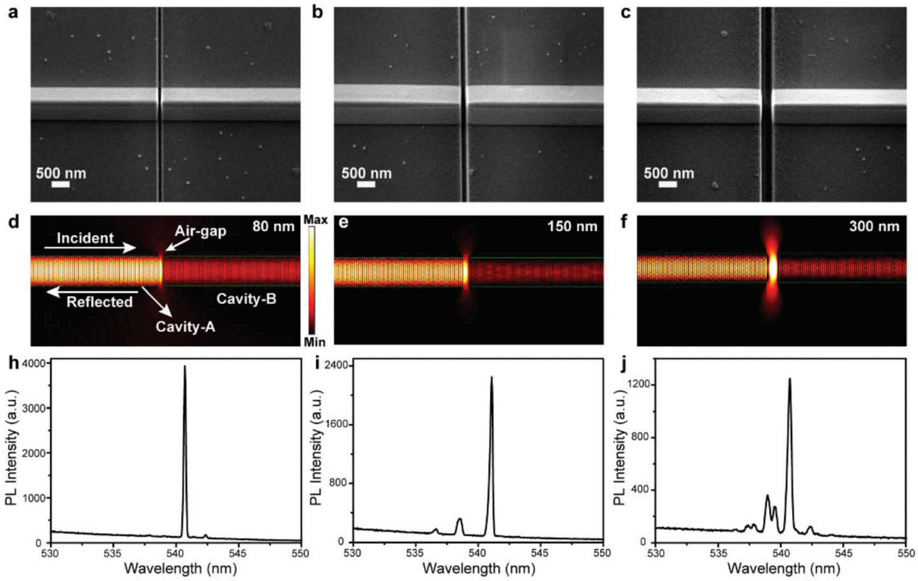

Fig. 4 (a–c) The SEM images of coupled cavity with the air-width of 80 nm, 150 nm and 300 nm, respectively. (d–f) The 2D electric field mappings of coupled cavity with the air-width of 80 nm, 150 nm and 300 nm, respectively. (h–j) The spectra of coupled cavity with the air-width of 80 nm, 150 nm and 300 nm, respectively.

for the coupled cavity. It can be found that the Q and P_{th} of the coupled cavity remain almost unchanged compared to the bare $CsPbBr_3$ NWs. Besides, we obtained a single-mode laser in other coupled cavities through the Vernier effect as well, as shown in Fig. S8.†

The width of the air-gap in coupled cavities plays a critical role in the lasing behavior, which is carefully studied. The light behavior in the F–P-type cavity can be described as follows: the light was confined in the NWs and oscillated along the NW axis and finally leaked out from the pair of end faces. The coupled cavity can be considered as two different FP cavities, which are aligned along the axis. When only cavity-A was excited, the light leaks out from near the air-gap end face of cavity-A; one part of the light is lost in scattering, and the other part is transmitted into cavity-B through the air gap. Previous research indicates that when the transmission of light from cavity-A into cavity-B is higher, the coupling is stronger, as well as the suppression of the laser modes is more efficient. In this experiment, we fabricated three different air-gaps with the width of 80 nm, 160 nm, and 300 nm, respectively, with the total length and length ratio unchanged, as shown in Fig. 4(a–c). The corresponding numerical simulations performed by the FDTD method are shown in Fig. 4(d–f), where more light is scattered outside by the wider air-gap with an increase in the air-gap width, and simultaneously less light is transmitted from cavity-A to cavity-B, which will lead to the reduction of the coupling efficiency. The corresponding spectra of the NW with the air-gaps of 80 nm, 150 nm, and 300 nm are given in Fig. 4(h–j), where the coupled cavity retained the single-mode laser output when the width of air-gap was increased to 80 nm, but the SMSR decreased to 17.2 dB. However, when the air-gap was increased to 150 nm, the coupling efficiency of coupled cavity decreased, leading to a multi-mode laser output. When the air-gap was further increased to 300 nm, cavity-A and cavity-B almost decoupled, which led to the multi-mode output. Based on the above discussion, there are two requirements for realizing the single-mode laser output in $CsPbBr_3$ NWs by the Vernier effect: a narrow enough air-gap to ensure coupling efficiency, and an appropriate ratio of cavity length to enable the FSR of coupled cavity to be higher than the medium gain range.

Conclusions

In conclusion, we prepared high-quality single crystal $CsPbBr_3$ perovskite NWs on a mica substrate by a typical CVD method in a controllable manner. A high quality single-mode laser is realized by designing and fabricating the coupled cavities by FIB milling based on the Vernier effect, showcasing a low threshold of ~20.1 μJ cm^{-2} and a high quality factor of ~2800. The influence of the air-gap width on the Vernier effect is studied by experiments and theoretical calculations, exhibiting that the coupling efficiency decreased and even decoupled with an increase in the air-gap. Meanwhile, the wavelength of the single-mode lasers can be adjusted by changing the length ratio of the coupling cavity. Our results may promote the application of perovskite NW lasers in optical communication and other photonic devices.

Author contribution

Fangtao Li: writing-original draft preparation, writing-review and editing, investigation, formal analysis, methodology, software. Mingming Jiang: simulation. Yang Cheng: investigation, methodology. Yufei Zhang: investigation, methodology. Yang Zheng: methodology, software. Yiyao Peng: investigation. Wenda Ma: investigation. Qiushuo Chen: investigation. Chunfeng Wang: investigation. Kaihui Liu: investigation. Rongming Wang: resources, validation, funding acquisition. Junfeng Lu: project administration, supervision. Caofeng Pan: project administration, resources, supervision, validation, funding acquisition.

Conflicts of interest

There are no conflicts to declare.

Acknowledgements

The authors thank the support of national key R & D project from Minister of Science and Technology, China (2018YFA0703702, 2016YFA0202703), National Natural Science Foundation of China (No. 51971025, 61675027, 51622205, 51432005, 61805015 and 61804011), Beijing City Committee of Science and Technology (Z171100002017019 and Z181100004418004), Beijing Natural Science Foundation (4181004, 4182080, 4184110, 2184131 and Z180011), Shenzhen Fundamental Research Project (JCYJ20190808170601664), and Shenzhen Science and Technology Program (Grant No. KQTD20170810105439418).

Notes and references

1 H. Gao, A. Fu, S. C. Andrews and P. Yang, *Proc. Natl. Acad. Sci. U. S. A.*, 2013, **110**, 865–869.
2 D. G. R. Yan and P. Yang, *Nat. Photonics*, 2009, **3**, 569–576.
3 S. W. Eaton, A. Fu, A. B. Wong, C. Z. Ning and P. Yang, *Nat. Rev. Mater.*, 2016, **1**, 16028.
4 J. Lu, C. Xu, F. Li, Z. Yang, Y. Peng, X. Li, M. Que, C. Pan and Z. L. Wang, *ACS Nano*, 2018, **12**, 11899–11906.
5 S. M. Michael, H. Huang, H. Feick, H. Yan, Y. Wu, H. Kind, E. Weber, R. Russo and P. Yang, *Science*, 2001, **282**, 1897–1899.
6 S. Makarov, A. Furasova, E. Tiguntseva, A. Hemmetter, A. Berestennikov, A. Pushkarev, A. Zakhidov and Y. Kivshar, *Adv. Opt. Mater.*, 2019, **7**, 1800784.
7 M. H. Zhuge, C. Pan, Y. Zheng, J. Tang, S. Ullah, Y. Ma and Q. Yang, *Adv. Opt. Mater.*, 2019, **7**, 1900275.

8 P. M. V. Alexander, S. Berestennikov, S. V. Makarov and Y. S. Kivshar, *Appl. Phys. Rev.*, 2019, **6**, 031307.

9 P. J. S. Pauzauskie, J. Donald and P. Yang, *Phys. Rev. Lett.*, 2006, **96**, 143903.

10 E. Y. T. Artem, S. Polushkin, A. P. Pushkarev and S. V. Makarov, *Nanophotonics*, 2020, **9**, 599–610.

11 Y. Xiao, C. Meng, P. Wang, Y. Ye, H. Yu, S. Wang, F. Gu, L. Dai and L. Tong, *Nano Lett.*, 2011, **11**, 1122–1126.

12 Q. Li, W. W. Chow, T. S. Luk, I. Brener, L. F. Lester and G. T. Wang, *Opt. Express*, 2012, **20**, 17873–17879.

13 A. Zhizhchenko, S. Syubaev, A. Berestennikov, A. V. Yulin, A. Porfirev, A. Pushkarev, I. Shishkin, K. Golokhvast, A. A. Bogdanov, A. A. Zakhidov, A. A. Kuchmizhak, Y. S. Kivshar and S. V. Makarov, *ACS Nano*, 2019, **13**, 4140–4147.

14 E. Tiguntseva, K. Koshelev, A. Furasova, P. Tonkaev, V. Mikhailovskii, E. V. Ushakova, D. G. Baranov, T. Shegai, A. A. Zakhidov, Y. Kivshar and S. V. Makarov, *ACS Nano*, 2020, **14**, 8149–8156.

15 Z. Liu, L. Yin, H. Ning, Z. Yang, L. Tong and C. Z. Ning, *Nano Lett.*, 2013, **13**, 4945–4950.

16 R. F. K. Charles and H. Henry, *IEEE J. Quantum Electron.*, 1984, **20**, 733–744.

17 J. Lu, Z. Yang, F. Li, M. Jiang, Y. Zhang, J. Sun, G. Hu, Q. Xu, C. Xu, C. Pan and Z. L. Wang, *Mater. Today*, 2018, **24**, 33–40.

18 Y. Xiao, C. Meng, X. Wu and L. Tong, *Appl. Phys. Lett.*, 2011, **99**, 023109.

19 B. Tang, H. Dong, L. Sun, W. Zheng, Q. Wang, F. Sun, X. Jiang, A. Pan and L. Zhang, *ACS Nano*, 2017, **11**, 10681–10688.

20 Z. Liu, J. Yang, J. Du, Z. Hu, T. Shi, Z. Zhang, Y. Liu, X. Tang, Y. Leng and R. Li, *ACS Nano*, 2018, **12**, 5923–5931.

21 Y. Wang, X. Li, V. Nalla, H. Zeng and H. Sun, *Adv. Funct. Mater.*, 2017, **27**, 1605088.

22 Y. Jia, R. A. Kerner, A. J. Grede, A. N. Brigeman, B. P. Rand and N. C. Giebink, *Nano Lett.*, 2016, **16**, 4624–4629.

23 Z. W. L. Feng, R. Ma, Y. Wang and X. Zhang, *Science*, 2014, **346**, 972–975.

24 F. Qian, Y. Li, S. Gradečak, H.-G. Park, Y. Dong, Y. Ding, Z. L. Wang and C. M. Lieber, *Nat. Mater.*, 2008, **7**, 701–706.

25 Z. Yang, J. Lu, M. ZhuGe, Y. Cheng, J. Hu, F. Li, S. Qiao, Y. Zhang, G. Hu, Q. Yang, D. Peng, K. Liu and C. Pan, *Adv. Mater.*, 2019, **31**, e1900647.

26 Y. Y. Wang, C. X. Xu, M. M. Jiang, J. T. Li, J. Dai, J. F. Lu and P. L. Li, *Nanoscale*, 2016, **8**, 16631–16639.

27 Y. Y. Mohd, S. Alias, T. K. Ng, I. Dursun, D. Shi, M. I. Saidaminov, D. Priante, O. M. Bakr and B. S. Ooi, *J. Phys. Chem. Lett.*, 2016, **7**, 137–142.

28 F. Li, J. Lu, Q. Zhang, D. Peng, Z. Yang, Q. Xu, C. Pan, A. Pan, T. Li and R. Wang, *Sci. Bull.*, 2019, **64**, 698–704.

29 Q. Zhang, R. Su, W. Du, X. Liu, L. Zhao, S. T. Ha and Q. Xiong, *Small Methods*, 2017, **1**, 1700163.

30 P. Fu, Q. Shan, Y. Shang, J. Song, H. Zeng, Z. Ning and J. Gong, *Sci. Bull.*, 2017, **62**, 369–380.

31 X. Jia, C. Zuo, S. Tao, K. Sun, Y. Zhao, S. Yang, M. Cheng, M. Wang, Y. Yuan, J. Yang, F. Gao, G. Xing, Z. Wei, L. Zhang, H. L. Yip, M. Liu, Q. Shen, L. Yin, L. Han, S. Liu, L. Wang, J. Luo, H. Tan, Z. Jin and L. Ding, *Sci. Bull.*, 2019, **64**, 1532–1539.

32 H. Dong, X. Liu, J. Yao and Y. Zhao, *Chem. Soc. Rev.*, 2020, **49**, 951–982.

33 M. L. P. Lu, H. Wang, N. Sui, Z. Shi, W. W. Yu and Y. Zhang, *InfoMat*, 2019, **1**, 430.

34 A. P. Schlaus, M. S. Spencer, K. Miyata, F. Liu, X. Wang, I. Datta, M. Lipson, A. Pan and X. Y. Zhu, *Nat. Commun.*, 2019, **10**, 265.

35 A. P. Pushkarev, V. I. Korolev, D. I. Markina, F. E. Komissarenko, A. Naujokaitis, A. Drabavicius, V. Pakstas, M. Franckevicius, S. A. Khubezhov, D. A. Sannikov, A. V. Zasedatelev, P. G. Lagoudakis, A. A. Zakhidov and S. V. Makarov, *ACS Appl. Mater. Interfaces*, 2019, **11**, 1040–1048.

36 S. W. Eaton, M. Lai, N. A. Gibson, A. B. Wong, L. Dou, J. Ma, L. W. Wang, S. R. Leone and P. D. Yang, *Proc. Natl. Acad. Sci. U. S. A.*, 2016, **113**, 1993–1998.

37 H. Zhou, S. Yuan, X. Wang, T. Xu, X. Wang, H. Li, W. Zheng, P. Fan, Y. Li, L. Sun and A. Pan, *ACS Nano*, 2017, **11**, 1189–1195.

38 Y. Fu, H. Zhu, C. C. Stoumpos, Q. Ding, J. Wang, M. G. Kanatzidis, X. Zhu and S. Jin, *ACS Nano*, 2016, **10**, 7963–7972.

39 L. Huang, Q. Gao, L. D. Sun, H. Dong, S. Shi, T. Cai, Q. Liao and C. H. Yan, *Adv. Mater.*, 2018, **30**, e1800596.

40 X. Wang, M. Shoaib, X. Wang, X. Zhang, M. He, Z. Luo, W. Zheng, H. Li, T. Yang, X. Zhu, L. Ma and A. Pan, *ACS Nano*, 2018, **12**, 6170–6178.

41 B. Tang, Y. Hu, J. Lu, H. Dong, N. Mou, X. Gao, H. Wang, X. Jiang and L. Zhang, *Nano Energy*, 2020, **7**, 1104641.

42 L. Dou, M. Lai, C. S. Kley, Y. Yang, C. G. Bischak, D. Zhang, S. W. Eaton, N. S. Ginsberg and P. Yang, *Proc. Natl. Acad. Sci. U. S. A.*, 2017, **114**, 7216–7221.

43 B. Zhou, H. Dong, M. Jiang, W. Zheng, L. Sun, B. Zhao, B. Tang, A. Pan and L. Zhang, *J. Mater. Chem. C*, 2018, **6**, 11740–11748.

44 B. Tang, Y. Hu, H. Dong, L. Sun, B. Zhao, X. Jiang and L. Zhang, *Angew. Chem., Int. Ed.*, 2019, **58**, 16134–16140.

45 Q. Zhang, R. Su, X. Liu, J. Xing, T. C. Sum and Q. Xiong, *Adv. Funct. Mater.*, 2016, **26**, 6238–6245.

46 Y. Wang, X. Sun, R. Shivanna, Y. Yang, Z. Chen, Y. Guo, G. C. Wang, E. Wertz, F. Deschler, Z. Cai, H. Zhou, T. M. Lu and J. Shi, *Nano Lett.*, 2016, **16**, 7974–7981.

47 M. I. Saidaminov, M. A. Haque, J. Almutlaq, S. Sarmah, X.-H. Miao, R. Begum, A. A. Zhumekenov, I. Dursun, N. Cho, B. Murali, O. F. Mohammed, T. Wu and O. M. Bakr, *Adv. Opt. Mater.*, 2017, **5**, 1600704.

48 E. Oksenberg, E. Sanders, R. Popovitz-Biro, L. Houben and E. Joselevich, *Nano Lett.*, 2017, **18**, 424–433.

49 P. Liu, X. He, J. Ren, Q. Liao, J. Yao and H. Fu, *ACS Nano*, 2017, **11**, 5766–5773.

50 K. Park, J. W. Lee, J. D. Kim, N. S. Han, D. M. Jang, S. Jeong, J. Park and J. K. Song, *J. Phys. Chem. Lett.*, 2016, **7**, 3703–3710.